Full field tabletop EUV coherent diffractive imaging in a transmission geometry

Bosheng Zhang,[1,*] Matthew D. Seaberg,[1] Daniel E. Adams,[1] Dennis F. Gardner,[1] Elisabeth R. Shanblatt,[1] Justin M. Shaw,[2] Weilun Chao,[3] Eric M. Gullikson,[3] Farhad Salmassi,[3] Henry C. Kapteyn,[1] and Margaret M. Murnane[1]

[1]JILA, University of Colorado, 440 UCB, Boulder, Colorado 80309-0440, USA
[2]Electromagnetics Division, NIST, Boulder, Colorado 80305-3328, USA
[3]Center for X-ray Optics, Lawrence Berkeley National Laboratory, Berkeley, CA 94720, USA

Abstract
We demonstrate the first general tabletop EUV coherent microscope that can image extended, non-isolated, non-periodic, objects. By implementing keyhole coherent diffractive imaging with curved mirrors and a tabletop high harmonic source, we achieve improved efficiency of the imaging system as well as more uniform illumination at the sample, when compared with what is possible using Fresnel zone plates. Moreover, we show that the unscattered light from a semi-transparent sample can be used as a holographic reference wave, allowing quantitative information about the thickness of the sample to be extracted from the retrieved image. Finally, we show that excellent tabletop image fidelity is achieved by comparing the retrieved images with scanning electron and atomic force microscopy images, and show superior capabilities in some cases.

1. Introduction

Coherent diffractive imaging (CDI) [1–6] is a powerful technique for imaging at the nanoscale. CDI enables near-wavelength-limited imaging, making this technique particularly attractive for use with large- and small-scale coherent extreme ultraviolet (EUV) [7–12] and X-ray sources [13], as well as with electron sources [14–16]. Also known as lensless imaging, CDI reconstructs both the amplitude and the phase of an object by using the information contained in the intensity of its far-field diffraction pattern. This is accomplished via iterative algorithms [17–20] which can retrieve the phase of the diffraction pattern, provided that the measured diffraction pattern satisfies an oversampling condition [21, 22]. Furthermore, images obtained using CDI can achieve near diffraction-limited resolution [2, 8, 11, 13]. This is in contrast to conventional EUV/X-ray microscopy using Fresnel zone plates (FZP), in which the resolution is limited by the width of the outermost zone. To date, CDI has been used to extract the structure and dynamics of a variety of objects, including biological samples [5,23], magnetic materials [24,25], strain fields inside a nanocrystal [26] and integrated circuits [27]. The first X-ray demonstration of CDI was at a synchrotron source in 1999 [2]. By 2007, it was possible to implement CDI using tabletop EUV sources, and in particular, fully spatially coherent high harmonic generation (HHG) beams [7, 28, 29]. More recently, by illuminating an object with a tabletop HHG source at a wavelength of 13 nm, a record 22 nm spatial resolution was achieved for a tabletop, full-field, photon-based microscope [11].

The oversampling condition of CDI means that the intensity (modulus square) of the diffraction field should be sampled at the Nyquist frequency or higher, corresponding to an oversampling by a factor of 2 of the field amplitude itself in the detector plane [21, 22]. This condition requires that the sample be isolated, which presents a severe limitation to this imaging method. However, several techniques have been developed to overcome this limitation, including ptychography CDI [30], keyhole CDI [31], and apertured illumination CDI [12]. In ptychography CDI, adapted from an electron beam technique and later demonstrated using a synchrotron light source [30], a beam is scanned across an object. The additional information provided by the

overlap between adjacent scans is then used to reconstruct one large field-of-view image. Keyhole CDI, first demonstrated using light from a synchrotron source, uses a FZP focusing optic with smaller diameter than the incident beam to confine the illumination on the sample [31]. Finally, apertured illumination CDI projects an image of an aperture onto the sample plane to ensure isolated illumination. This technique requires high quality focusing optics and also a precise determination of the imaging plane of the aperture, and has been demonstrated using a He-Ne laser [12].

In this paper, we demonstrate the first tabletop EUV microscope that can image extended, non-isolated, non-periodic, objects by implementing keyhole CDI using a tabletop EUV source. We also significantly increase the utility of keyhole CDI by using a curved EUV mirror instead of a FZP to focus the light onto the sample. This approach has three major advantages: first, it represents the first general tabletop full field EUV coherent microscope; second, it demonstrates higher photon flux throughput relative to a FZP at the illumination wavelength of 29 nm; and third, it produces a more uniform illumination on the sample since there is no need for a central beam stop when a curved focusing optic is used. To demonstrate the power of this approach, we use keyhole CDI to image a semi-transparent sample and show that depth information can be obtained by using the un-scattered light as the reference beam of an in-line hologram [32]. Finally, we show that excellent image fidelity is achieved by comparing the retrieved images with scanning electron and atomic force microscopy images. In comparison with AFM, our tabletop CDI approach requires no contact with samples and is non-destructive. In comparison with SEM, which cannot penetrate thick samples, tabletop CDI can image 3D features through a sample.

2. Keyhole CDI of an extended aperiodic sample with an opaque background

First, we demonstrated keyhole CDI with a tabletop HHG EUV source using a sample with an opaque background. A schematic diagram of the setup in the imaging chamber is shown in Fig. 1(a). We focused a 25 fs pulse duration, 1 mJ pulse energy, 3 kHz repetition-rate, Ti:sapphire laser beam with wavelength centered around 780 nm, into a 150 μm diameter hollow waveguide filled with Ar gas to generate phase-matched, spatially coherent, harmonics at wavelengths near 29 nm. After the waveguide, the HHG beam and CDI microscope were in medium vacuum (≈ 10^{-6} torr) to avoid absorption of the EUV light from air. We used a pair of silicon mirrors oriented at near the Brewster's angle for the 780 nm light to effectively absorb the unconverted 780 nm light while reflecting the EUV beam. The 780 nm light was further filtered out by two 200 nm thick aluminum filters. The harmonics of only odd orders [33] are separated in energy by about 3 eV (twice of the fundamental 780 nm photon energy), and only one harmonic (27th order) was selected and focused on the sample with a flat and a curved EUV multilayer mirror (radius of curvature 25 cm). The EUV mirrors have a full width at half maximum (FWHM) bandwidth of 2.1 eV centered around 43.2 eV (corresponding to a wavelength of λ = 28.7 nm). Typically, a single EUV harmonic at this photon energy has a FWHM bandwidth of about 0.4 eV (a representative spectrum of EUV harmonics can be found in [34]), corresponding to a longitudinal coherence length of $L_c = \lambda^2/\Delta\lambda$ = 3.1 μm. This means that for a field of view (FOV) D at the sample, the maximum scattering angle θ_{max}, limited by finite L_c, is determined by $\tan\theta_{max} = 2L_c/D$ (See [35]. Notice here we use a different definition of L_c, and do not use the approximation of $\tan\theta \approx \theta$ when θ is small). For all the experiments performed in this paper, $D \leq 25$ μm. For D = 25 μm, the NA is required to be ≤ 0.3, which is greater than the experimental NA used in this section (0.23) as well as that in next section (0.20).

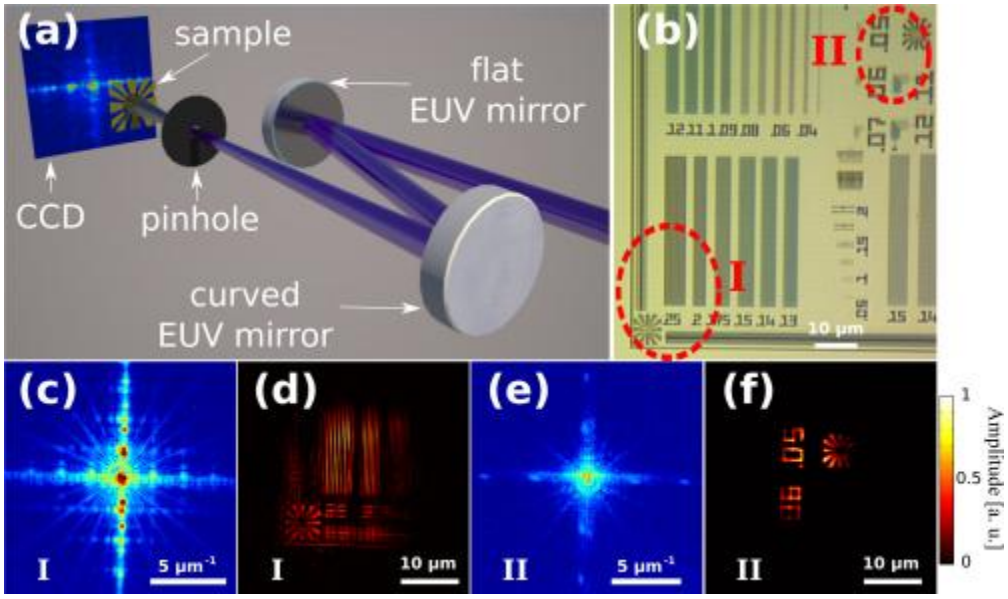

Fig. 1 Tabletop EUV keyhole CDI of a sample with an opaque background. (a) Setup in the CDI vacuum chamber. The EUV mirror with a 25 cm radius of curvature focuses the HHG beam, and puts a curved wavefront on the sample. A pinhole placed before the x- and y-foci introduces a sharp edge onto the beam. (b) Image of the sample using a high magnification optical microscope. Two regions of interest, I and II, are circled, with corresponding measured diffraction patterns (cropped and centered) shown in (c) and (e), and their corresponding reconstructions of the electric field amplitude (normalized to unity at maximum with arbitrary units) shown in (d) and (f). The color map as shown on the right of (f) is shared by (d) and (f).

The EUV mirror pair has generally higher throughput than the FZP used in conventional keyhole CDI, while also inducing a curved wavefront that is very beneficial for the reconstruction algorithm [36]. The non-normal incidence of the HHG beam on the EUV curved mirror produces some astigmatism in the beam. A 50 μm diameter pinhole was placed about 2 mm before the horizontal focus (x-focus) to introduce a sharp edge on the HHG beam and enforce the isolation requirement on the illumination, rather than the sample. We measured the positions of the x-focus and y-focus with ±50 μm accuracy by use of the pinhole as a knife-edge scanner. The separation of x-focus and y-focus was measured to be ≈ 0.55 mm. The sample was composed of a 100 nm thick gold layer (which has a negligible transmission of 5×10^{-5} for 28.7 nm light), deposited on a thin Si_3N_4 membrane. Features were etched into the gold layer, as shown in the dark areas in Fig. 1(b). Keyhole CDI enables the imaging of any region of interest on such an extended sample; here we selected region I and region II as indicated in Fig. 1(b). The imaging FOV can be adjusted by placing the sample at different distances from the focus positions, which corresponds to different HHG beam spot sizes. For the measured diffraction shown in Figs. 1(c) (for region I) and 1(e) (for region II), the sample was placed 1.3 mm and 0.9 mm downstream of the circle of least confusion (the midpoint of x- and y- foci) respectively, resulting in a FOV of $D \approx 25$ μm and $D \approx 18$ μm. The diffraction patterns were recorded on an X-ray CCD (Andor iKon-L, 2048 × 2048 pixel array, 13.5 × 13.5 μm^2 pixel size), as shown in Figs. 1(c) and 1(e), with a total exposure time of 30 minutes for each. The CCD was positioned at a distance of 44.6 mm from the circle of least confusion.

When performing an image reconstruction, it is important to note that the reconstruction actually represents what is know as the exit-surface wave (ESW):

$$E_{t,\mathrm{Smp}}(x',y') = E_{i,\mathrm{Smp}}(x',y')\,t(x',y'), \tag{1}$$

where $E_{i,\mathrm{Smp}}(x', y')$ is the incident field at the position (x', y') on the sample plane, and $t(x', y')$ is the complex transmission function. This simple modeling of the ESW as the complex multiplication of the incident beam and the sample complex transmission function is valid when $\Delta z \ll D/\mathrm{NA}$, where Δz is the thickness of the sample (see [37], supporting material). For experiments performed in this section, NA ≈ 0.23, and the calculated D/NA is 104 μm for Fig. 1(c) and 75 μm for Fig. 1(e), both of which are much greater than the thickness of the sample (≈ 150 nm), so Eq. (1) is valid. The electric field at (x, y) position on the detector plane is given in the paraxial Fresnel approximation by

$$E_{t,\mathrm{Det}}(x,y)=e^{i2\pi\lambda z}i\lambda z e^{i\pi\lambda z(x^2+y^2)}\iint_{-\infty}^{\infty} e^{-i2\pi\lambda z(xx'+yy')}e^{i\pi\lambda z(x'^2+y'^2)}E_{t,\mathrm{Smp}}(x',y')\,\mathrm{d}x'\,\mathrm{d}y', \quad (2)$$

where z is the distance between the sample and the detector [38]. In the case of a binary sample with an opaque background level as used in this experiment, if we let t_c be the constant transmission value for the feature area, then $t(x', y')$ can be written as $t(x', y') = |t(x', y')|\exp(i\phi t_c)$, where ϕ_A denotes the phase of a complex quantity A. Then Eq. (2) is equivalent to

$$U = \mathcal{F}[e^{i\pi\lambda z(x'^2+y'^2)}e^{i\phi_{Ei,\mathrm{Smp}}(x',y')}u(x',y')], \quad (3)$$

where U is defined as $U=E_{t,\mathrm{Det}}(x,y)\{1i\lambda z\exp[i2\pi\lambda z+i\pi\lambda z(x2+y2)+i\phi t_c]\}-1$, having an amplitude proportional to the measured $|E_{t,\mathrm{Det}}|$, $\mathcal{F}$ is the Fourier transform, and $u(x', y') = |E_{i,\mathrm{Smp}}(x', y')t(x', y')|$ is the quantity to be reconstructed. This equation provides the required transform that relates the detector plane to the sample plane. The precise characterization of the incident beam $E_{i,\mathrm{Smp}}$ is possible through techniques such as ptychography CDI [37]; in this paper, we use an approximation: we consider only the quadratic phase (including astigmatism) while ignoring higher order phases, thus $Ei,\mathrm{Det}=|Ei,\mathrm{Det}|\exp[i\pi\lambda(x2/z\mathrm{dfx}+y2/z\mathrm{dfy})]$, where $|E_{i,\mathrm{Det}}|$ is the measured amplitude of the beam (with the sample out of the beam path) on the detector, z_{dfx} is the distance between the detector and the x-focus, and z_{dfy} is the distance between the detector and the y-focus. We then back-propagated $E_{i,\mathrm{Det}}$ to the sample plane to obtain $E_{i,\mathrm{Smp}}$. Reconstruction of u was conducted using a modified RAAR algorithm [19]. We started from an initial guess of random phase for the diffracted wave, and each iteration was composed of the following three steps:

1. Calculate u using the inverse transform for Eq. (3): $u=\exp[-i\pi\lambda z(x'2+y'2)-i\phi Ei,\mathrm{Smp}(x',y')]F-1U$;
2. Apply the support constraint provided by the finite illumination, and a constraint of the phase of u to be within $[-\pi/4, \pi/4]$ rad, which is equivalent to the non-negativity constraint [39];
3. Calculate U using the transform defined in Eq. (3) and apply the modulus constraint.
4. The algorithm iterates until a suitably low error is achieved or more importantly, the derivative of the error reaches a constant value; usually below 100 iterations. After the algorithm converged, 100 iterations were averaged together to produce the object domain reconstructions, as shown in Figs. 1(d) and (f) for region I and II respectively. Based on Abbe Theory [40], the theoretical resolution achieved in this first demonstration is $0.82\lambda/\mathrm{NA}$ = 102 nm, which can be easily improved in the future by use of a shorter wavelength illumination or by increasing the NA.
5. The original implementation of keyhole CDI [31] made use of a FZP with a smaller diameter than the incident beam to constrain the extent of the illumination on the sample. A central beam-stop is required in this case, in order to prevent any unfocused

light from illuminating the sample. This results in an annular beam. In the implementation of keyhole CDI discussed here, the FZP is replaced by a curved EUV multilayer mirror, which is generally more efficient. A detailed discussion of the efficiency of EUV zone plates can be found in [41]. An ideal (without fabrication imperfections, with no substrate that introduces extra absorption) FZP of alternately opaque and transmissive zones has a theoretical efficiency (diffracted into +1 order) of $1/\pi^2 \approx 10\%$; while for an ideal phase reversal zone plate, the theoretical efficiency is $4/\pi^2 \approx 41\%$. Due to absorption of materials for the EUV wavelength, it is not possible to build a genuine phase reversal zone plate with transparent phase-shifting zones. Based on the results and with materials that "seem suitable" from [41], for 28.7 nm as used in this paper, an ideal FZP made of aluminum, assuming no oxidation in addition, has a calculated efficiency of 28%; while for 13 nm (the wavelength used in EUV lithography), an ideal FZP made of beryllium has a calculated efficiency of 24%. The efficiency will be even less for implementation in keyhole CDI due to the use of the central beam-stop. In comparison, our 28.7nm EUV mirror has a measured efficiency of 47%, and the 13 nm EUV mirror has a measured efficiency of 66%. In addition to the improved efficiency, EUV-mirror-based keyhole CDI does not require a central beam-stop; therefore the sample is more uniformly illuminated. To our knowledge, these results represent the first demonstration of a general and efficient tabletop coherent EUV microscope that can image extended (i.e. non-isolated) samples, as well as the first demonstration of keyhole CDI using a tabletop EUV source.

3. Keyhole CDI for a sample with a semi-transparent background

Next we performed EUV-mirror-based keyhole CDI on a sample with a semi-transparent background (Fig. 2). The HHG source and EUV mirrors were similar to those used in the previous measurements but with some improvements, such as the use of a higher laser repetition-rate of 5 kHz, and a larger, 200-μm-diameter waveguide. These improvements resulted in an enhancement of the HHG flux from $\approx 10^9$ to $\approx 10^{10}$ photons per second in a single harmonic at the exit of the waveguide. For the sample used in this section, which has less scattering efficiency than the previous sample, these improvements decrease the required exposure times for this experiment from about 2 hours to 14 minutes.

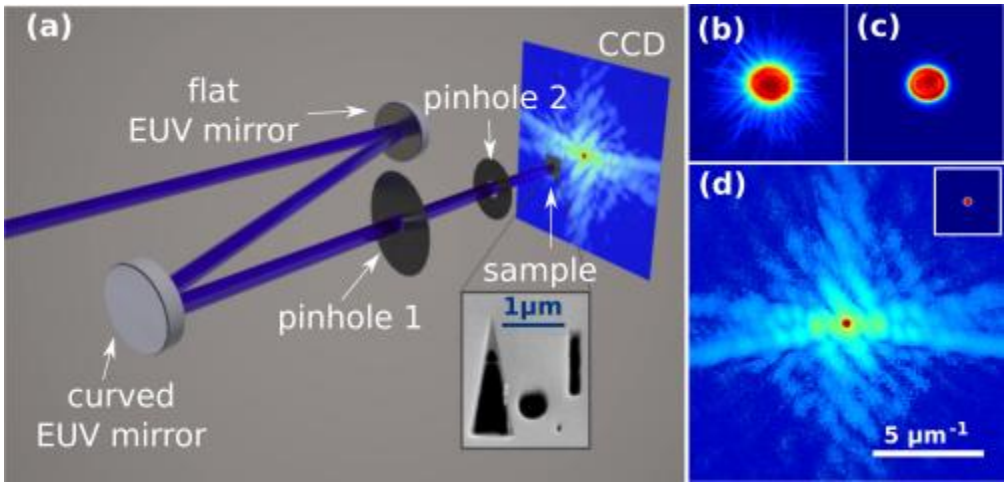

Fig. 2 Tabletop EUV keyhole CDI of a sample with a semi-transparent background. (a) Schematic of the setup. A second pinhole is inserted into the beam to remove scatter light form the first pinhole. The inset shows an SEM image of the sample, composed of a 30 nm Cr film deposited on top of a 45-nm-thick Si_3N_4 membrane. (b) and (c) A

zoomed view of the beam on the CCD before and after inserting the second pinhole. (d) Diffraction pattern (cropped and centered) from the sample shown to the 1/4 power. The inset shows the diffraction pattern of the beam when the sample is removed.

The second sample consists of 30 nm chromium deposited on a 45-nm-thick Si_3N_4 membrane. The patterned features, etched in the Cr/Si_3N_4 sample by use of focused ion beam, are shown in the inset SEM image of Fig. 2(a). Unlike the first sample, this sample was ≈ 8.5% transparent. As a result, the diffraction pattern contains a large amount of un-scattered light.
As discussed above, the non-normal incidence of the EUV beam on the curved mirror introduced astigmatism, with a separation between horizontal and vertical foci of 1.5 mm in this case. To implement keyhole CDI, a 200-μm-diameter pinhole aperture was placed in the beam 16 mm upstream of the circle of least confusion. Due to the transparent nature of this sample, the scattered light from the aperture was of similar amplitude to that from the sample and had to be removed. To accomplish this, a second 50 μm diameter pinhole aperture was placed between the first aperture and the sample to spatially filter most of the unwanted scattered light from the hard edge of the first pinhole (see the sketch of the experimental setup in Fig. 2(a)). This second aperture was placed 1.4 mm upstream of the circle of least confusion. As shown in Figs. 2(b) and 2(c), the second aperture removed the majority of the unwanted light scattered from the first aperture. The sample as positioned at the circle of least confusion, where the illumination spot size was 8 μm in diameter. The detector was placed 5.71 cm away from the sample. The measured diffraction patterns of the sample and the beam are shown in Fig. 2(d) and its inset, respectively, corresponding to an NA = 0.20, leading to a theoretical resolution of $0.82\lambda/\mathrm{NA} = 118$ nm.

In this experiment, the thickness of the sample(≈ 75 nm) is much less than $D/\mathrm{NA} = 40$ μm, so Eq. (1) is again valid. We write the total complex transmission function as: $t(x', y') = t_0(x', y') + \Delta t(x', y')$, where $t_0(x', y')$ is the transmission coefficient of the background unpatterned Cr/Si_3N_4 layers of the sample (≈ 0.29), and $\Delta t(x', y')$ is the modification to the transmission of the sample due to the etched features. This reconstruction approach is similar to that used in Fresnel CDI [42]. We write $U=\mathrm{F}\{\exp[i\pi\lambda z(x'2+y'2)]Ei,\mathrm{Smp}(1+\Delta t(x',y')t0(x',y'))\}$ where U has the magnitude proportional to the measured magnitude of the electric field at the detector, and $\Delta t/t_0$ is the quantity to be reconstructed in the iterative algorithm. We first calculated the incident field $E_{i,\mathrm{Smp}}$ using the same approach explained in [43], with the sagittal and tangential slices through the propagated beam shown in Figs. 3(a) and 3(b). The quantity $\Delta t/t_0$ is non-zero only in the feature areas, allowing us to use the shrink-wrap dynamic support constraint [20]. An additional constraint on the phase of $\Delta t/t_0$ to be within $[\phi_0 - \Delta\phi/2, \phi_0 + \Delta\phi/2]$, where $\phi_0 = 2.0$ rad and $\Delta\phi = \pi/2$ rad were determined empirically, was found to significantly speed up the convergence of the iterative reconstruction. The magnitude of t_0 was determined from the ratio of the beam intensity on the CCD with the sample's Cr/Si_3N_4 layers in the beam and that of the sample out of the way. Starting with an initial guess of random phase on the detector, we typically used 20 to 100 iterations of the RAAR algorithm [17] followed by 10 iterations of the error reduction algorithm [18] to retrieve the sample diffraction phase on the detector. We averaged over 10 independent reconstructions, and the amplitude (normalized) $||\Delta tt0||$ and phase $\phi_t(x', y')$ (the phase of the background is chosen as the zero-phase reference), shown in Figs. 3(e) and 3(f), are in very good agreement with the SEM images shown in Figs. 3(c) (top) and 3(d) (bottom). Moreover, it was also possible to reconstruct the image of the small 50-nm-diameter hole, seen in the topside SEM image Fig. 3(c).

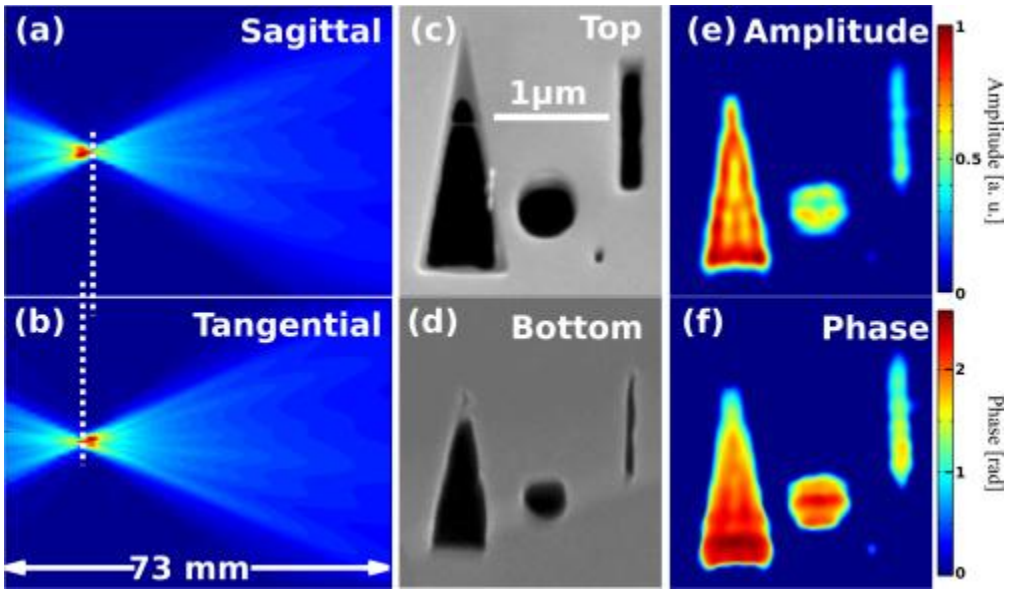

Fig. 3 (a),(b) Sagittal and tangential slices through the focusing EUV beam. The dashed lines show the positions of the two foci. (c) SEM image of the top side of the sample (geometrically scaled to account for a 52° tilt of the sample plane). (d) SEM image of the bottom side of the sample. Only the darkest parts on the sample are completely etched through. (e), (f) Reconstructed amplitude (normalized to unity at maximum with arbitrary units) $||\Delta tt0||$ and phase ϕ_t (x', y') of the sample. (d) (e) (f) have the same scale bar as (c).

The ESW can be written as $E_t = E_i(t_0 + \Delta t)$. We see that a non-zero transmission factor t_0 produces a reference wave while Δt produces an object wave for the in-line holography geometry [31,44]. Thus, for the sample used in this experiment, the diffraction pattern in Fig. 2(d) is in actuality an in-line hologram. However, since there is only a small area on the CCD where the reference wave has significant intensity to produce interference with the scattered wave from the sample, the image from a conventional in-line holographic reconstruction [44,45] would not have the same high resolution as CDI. Moreover, in-line holographic reconstructions also suffer from twin-image artifacts [46]. Using the known reference wave, CDI can be used to extract phase information about the object. Furthermore, with this extracted phase information, and the value(s) of index of refraction for the material, we can obtain thickness or depth information.

A reference topography measurement of the sample is shown in Fig. 4(a) by use of a Digital Instruments Dimension 3100 atomic force microscope (AFM), with a probe tip size of 3 nm and a scan step size of 16 nm. By comparison, we then calculate the depth map from the keyhole CDI reconstruction. For the sample used in this experiment, if we define the top plane (completely unetched) as the zero depth level, and write the index of refraction for EUV as $n = 1 - \delta + i\beta$, then the phase of t as a function of the depth d (≤ 0) can be written as

$$\phi t(d)=\begin{cases} -2\pi\lambda\delta\mathrm{Cr}\cdot d & \text{for } -h\mathrm{Cr}\leq d\leq 0, \\ -2\pi\lambda[\delta\mathrm{Cr}\cdot(-h\mathrm{Cr})+\delta\mathrm{Si3N4}\cdot(d+h\mathrm{Cr})] & \text{for } d\leq -h\mathrm{Cr}, \end{cases} \quad (4)$$

where h_{Cr} is the thickness of the top Cr layer. The deposited Cr film has a density of 6.55 g/cm^3 (8.9% less than the bulk Cr density 7.19 g/cm^3), determined from an X-ray reflectivity measurement. By use of the known δ_{Cr} and δ_{Si3N4} values at the illuminating wavelength [47], as well as h_{Cr} = 30 nm, we calculated the depth map of the sample from the reconstructed phase ϕ_t

with Eq. (4). To determine the uncertainty of our quantitative analysis, we considered the major error sources. First, the ±50 μm uncertainty in determining the positions of the two astigmatic foci results in an error in the calculated phase of the incident beam and thus the reconstructed sample phase and thickness. Second, the uncertainty in the wavelength (28.7 ± 0.7 nm due to the bandwidth of the multilayer mirrors) causes uncertainty in the values of index of refraction, leading to error in the thickness calculation. Third, the imperfect repeatability of reconstructions leads to small fluctuations in the calculations. We scanned the focus positions and the wavelength in their uncertainty range, and for each parameter set, we performed 10 independent reconstructions; from all reconstructions, we found the maximum and minimum depth at each position, with the mean values shown in Fig. 4(b). An AFM is a surface measurement device, meaning that those portions of the sample that are completely etched through will result in an artificially deep measurement. We find, using −75 nm as the lower threshold, that the AFM image gives the same shape in the completely etched regions as the SEM image of the bottom side of the sample, as shown in Fig. 3(d). These images confirm that the 50 nm wide hole and the edges of the larger features are not fully etched through. Fig. 4(c) compares the depth profiles along the dashed lines in Fig. 4(b) between keyhole CDI and AFM. The error bars plotted in Fig. 4(c) indicate the maximum and minimum depth values found within the range of uncertainty. We see good quantitative agreement between the AFM and tabletop EUV keyhole CDI images. The depth of the 50 nm wide hole is 20 ± 5 nm as measured by AFM, and 28 ± 9 nm from keyhole CDI. The AFM uncertainty of ±5 nm is determined from a two-dimensional grating calibration standard with a 180 nm step height, and is given for a 95% confidence level.

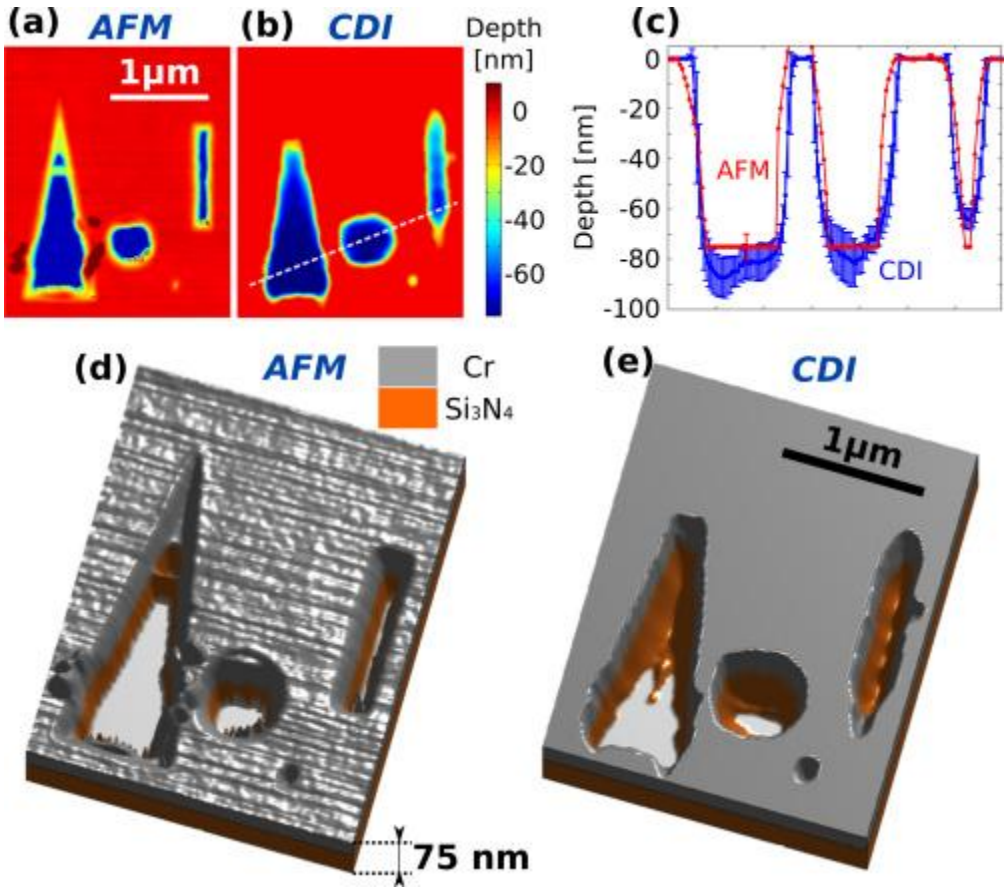

Fig. 4 (a), (b) Depth maps of the sample using AFM and keyhole CDI respectively. (c) Comparison of lineouts along the dashed line in (b) with associated error bars. (d) and (e) 3D profiles of the sample based on the depth values in (a) and (b). The top 30 nm Cr layer and bottom 45 nm Si_3N_4 layer are shown in different colors.

Keyhole CDI illuminated by EUV high harmonics has several advantages in comparison with AFM. First, the depth profile from the entire FOV can be measured simultaneously so that point-by-point scanning is unnecessary. Thus, there is the potential for much higher data acquisition speeds, limited only by the illumination flux. Second, AFM images can be influenced by nonlinearity, hysteresis, creep of the piezoelectric material, and cross-talk between the x, y, and z axes. In practice, software enhancement and filtering are used to improve AFM image quality, but this post-processing can also flatten out real topographical features. Keyhole CDI has no such problems. Third, keyhole CDI allows a long working distance and no contact with the sample, thus avoiding potential sample damage. A limitation of our current technique is that it is only applicable to relatively thin samples; the sample should be thin enough so that the light can penetrate, and much thinner than *D*/NA as mentioned before. However, this limitation can be overcome in the future by extending tabletop keyhole CDI to reflection mode [12].

4. Conclusion

Using a new approach to keyhole coherent diffractive imaging, we have demonstrated a tabletop EUV microscope that can image extended, non-isolated, aperiodic samples for the first time. We achieve increased efficiency of the imaging system and a more uniform illumination at the sample when compared with previously reported methods based on Fresnel zone plates. Quantitative depth information about the object can also be retrieved, in very good agreement with AFM measurements and with significant added benefits such as non-contact, non-destructive measurement capabilities. In the future, when combined with advances in bright HHG sources with < 1 nm wavelength [33], this approach can be used to image nanoscale dynamics, including ultrafast spin, heat, strain and current flow [48–50] with combined few femtosecond time resolution and sub-10 nm spatial resolution, in thick samples, with elemental and chemical sensitivity.

Acknowledgments

We thank David Alchenberger for assistance in acquiring the AFM image and Paul Rice for use of the focused ion beam system. We also gratefully acknowledge support from a National Security Science and Engineering Faculty Fellowship and from the National Science Foundation Engineering Research Center in EUV Science and Technology. M. Seaberg, D. Gardner, and E. Shanblatt acknowledge support from an NSF IGERT program.

References and links

1. J. N. Cederquist, J. R. Fienup, J. C. Marron, and R. G. Paxman, “Phase retrieval from experimental far-field speckle data,” Opt. Lett. **13**, 619–621 (1988).
2. J. Miao, P. Charalambous, J. Kirz, and D. Sayre, “Extending the methodology of X-ray crystallography to allow imaging of micrometre-sized non-crystalline specimens,” Nature **400**, 342–344 (1999).
3. I. Robinson, I. Vartanyants, G. Williams, M. Pfeifer, and J. Pitney, “Reconstruction of the Shapes of Gold Nanocrystals Using Coherent X-Ray Diffraction,” Phys. Rev. Lett. **87**,

195505 (2001).

4. G. Williams, M. Pfeifer, I. Vartanyants, and I. Robinson, “Three-Dimensional Imaging of Microstructure in Au Nanocrystals,” Phys. Rev. Lett. **90**, 175501 (2003).
5. D. Shapiro, P. Thibault, T. Beetz, V. Elser, M. Howells, C. Jacobsen, J. Kirz, E. Lima, H. Miao, A. M. Neiman, and D. Sayre, “Biological imaging by soft x-ray diffraction microscopy.” Proc. Natl. Acad. Sci. U.S.A. **102**, 15343–15346 (2005).
6. H. N. Chapman, A. Barty, M. J. Bogan, S. Boutet, M. Frank, S. P. Hau-Riege, S. Marchesini, B. W. Woods, S. Bajt, W. H. Benner, R. A. London, E. Plönjes, M. Kuhlmann, R. Treusch, S. Düsterer, T. Tschentscher, J. R. Schneider, E. Spiller, T. Möller, C. Bostedt, M. Hoener, D. A. Shapiro, K. O. Hodgson, D. van der Spoel, F. Burmeister, M. Bergh, C. Caleman, G. Huldt, M. M. Seibert, F. R. N. C. Maia, R. W. Lee, A. Szöke, N. Timneanu, and J. Hajdu, “Femtosecond diffractive imaging with a soft-X-ray free-electron laser,” Nat. Phys. **2**, 839–843 (2006).
7. R. Sandberg, A. Paul, D. Raymondson, S. Hädrich, D. Gaudiosi, J. Holtsnider, R. Tobey, O. Cohen, M. Murnane, H. Kapteyn, C. Song, J. Miao, Y. Liu, and F. Salmassi, “Lensless Diffractive Imaging Using Tabletop Coherent High-Harmonic Soft-X-Ray Beams,” Phys. Rev. Lett. **99**, 098103 (2007).
8. R. L. Sandberg, C. Song, P. W. Wachulak, D. A. Raymondson, A. Paul, B. Amirbekian, E. Lee, A. E. Sakdinawat, C. La-O-Vorakiat, M. C. Marconi, C. S. Menoni, M. M. Murnane, J. J. Rocca, H. C. Kapteyn, and J. Miao, “High numerical aperture tabletop soft x-ray diffraction microscopy with 70-nm resolution.” Proc. Natl. Acad. Sci. U.S.A. **105**, 24–27 (2008).
9. R. L. Sandberg, D. A. Raymondson, C. La-O-Vorakiat, A. Paul, K. S. Raines, J. Miao, M. M. Murnane, H. C. Kapteyn, and W. F. Schlotter, “Tabletop soft-x-ray Fourier transform holography with 50 nm resolution.” Opt. Lett. **34**, 1618–1620 (2009).
10. R. A. Dilanian, B. Chen, G. J. Williams, H. M. Quiney, K. A. Nugent, S. Teichmann, P. Hannaford, L. V. Dao, and A. G. Peele, “Diffractive imaging using a polychromatic high-harmonic generation soft-x-ray source,” J. Appl. Phys. **106**, 023110 (2009).
11. M. D. Seaberg, D. E. Adams, E. L. Townsend, D. A. Raymondson, W. F. Schlotter, Y. Liu, C. S. Menoni, L. Rong, C.-C. Chen, J. Miao, H. C. Kapteyn, and M. M. Murnane, “Ultrahigh 22 nm resolution coherent diffractive imaging using a desktop 13 nm high harmonic source.” Opt. Express **19**, 22470–22479 (2011).
12. D. F. Gardner, B. Zhang, M. D. Seaberg, L. S. Martin, D. E. Adams, F. Salmassi, E. Gullikson, H. Kapteyn, and M. Murnane, “High numerical aperture reflection mode coherent diffraction microscopy using off-axis apertured illumination.” Opt. Express **20**, 19050–19059 (2012).
13. H. N. Chapman and K. A. Nugent, “Coherent lensless X-ray imaging,” Nat. Photonics **4**, 833–839 (2010).
14. U. Weierstall, Q. Chen, J. C. Spence, M. R. Howells, M. Isaacson, and R. R. Panepucci, “Image reconstruction from electron and X-ray diffraction patterns using iterative algorithms: experiment and simulation.” Ultramicroscopy **90**, 171–195 (2001)
15. J. M. Zuo, I. Vartanyants, M. Gao, R. Zhang, and L. A. Nagahara, “Atomic resolution imaging of a carbon nanotube from diffraction intensities.” Science **300**, 1419–1421 (2003).
16. M. J. Humphry, B. Kraus, A. C. Hurst, A. M. Maiden, and J. M. Rodenburg, “Ptychographic electron microscopy using high-angle dark-field scattering for sub-nanometre resolution imaging.” Nat. Commun. **3**, 730 (2012).
17. D. R. Luke, “Relaxed averaged alternating reflections for diffraction imaging,” Inverse Prob. **21**, 37–50 (2005).

18. J. R. Fienup, “Phase retrieval algorithms: a comparison.” Appl. Opt. **21**, 2758–2769 (1982).
19. D. E. Adams, L. S. Martin, M. D. Seaberg, D. F. Gardner, H. C. Kapteyn, and M. M. Murnane, “A generalization for optimized phase retrieval algorithms.” Opt. Express **20**, 24778–24790 (2012).
20. S. Marchesini, H. He, H. N. Chapman, S. P. Hau-Riege, A. Noy, M. R. Howells, U. Weierstall, and J. C. H. Spence, “X-ray image reconstruction from a diffraction pattern alone,” Phys. Rev. B **68**, 140101 (2003).
21. R. H. T. Bates, “Fourier phase problems are uniquely solvable in more than one dimension. I: Underlying theory,” Optik **61**, 247–262 (1982).
22. J. Miao, D. Sayre, and H. N. Chapman, “Phase retrieval from the magnitude of the Fourier transforms of nonperiodic objects,” J. Opt. Soc. Am. A **15**, 1662 (1998).
23. J. Miao, T. Ishikawa, Q. Shen, and T. Earnest, “Extending X-ray crystallography to allow the imaging of non-crystalline materials, cells, and single protein complexes.” Annu. Rev. Phys. Chem. **59**, 387–410 (2008).
24. P. Fischer, “Studying nanoscale magnetism and its dynamics with soft X-ray microscopy,” IEEE Trans. Magn. **44**, 1900–1904 (2008).
25. A. Tripathi, J. Mohanty, S. H. Dietze, O. G. Shpyrko, E. Shipton, E. E. Fullerton, S. S. Kim, and I. McNulty, “Dichroic coherent diffractive imaging.” Proc. Natl. Acad. Sci. U.S.A. **108**, 13393–13398 (2011).
26. M. A. Pfeifer, G. J. Williams, I. A. Vartanyants, R. Harder, and I. K. Robinson, “Three-dimensional mapping of a deformation field inside a nanocrystal.” Nature **442**, 63–66 (2006).
27. B. Abbey, G. J. Williams, M. A. Pfeifer, J. N. Clark, C. T. Putkunz, A. Torrance, I. McNulty, T. M. Levin, A. G. Peele, and K. A. Nugent, “Quantitative coherent diffractive imaging of an integrated circuit at a spatial resolution of 20 nm,” Appl. Phys. Lett. **93**, 214101 (2008).
28. A. Rundquist, C. G. Durfee, Z. Chang, C. Herne, S. Backus, M. M. Murnane, and H. C. Kapteyn, “Phase-matched generation of coherent soft X-rays,” Science **280**, 1412–1415 (1998).
29. R. A. Bartels, A. Paul, H. Green, H. C. Kapteyn, M. M. Murnane, S. Backus, I. P. Christov, Y. Liu, D. Attwood, and C. Jacobsen, “Generation of spatially coherent light at extreme ultraviolet wavelengths,” Science **297**, 376–378 (2002).
30. J. Rodenburg, A. Hurst, A. Cullis, B. Dobson, F. Pfeiffer, O. Bunk, C. David, K. Jefimovs, and I. Johnson, “Hard-X-Ray Lensless Imaging of Extended Objects,” Phys. Rev. Lett. **98**, 034801 (2007).
31. B. Abbey, K. A. Nugent, G. J. Williams, J. N. Clark, A. G. Peele, M. A. Pfeifer, M. de Jonge, and I. McNulty, “Keyhole coherent diffractive imaging,” Nat. Phys. **4**, 394–398 (2008).
32. J. N. Clark, C. T. Putkunz, E. K. Curwood, D. J. Vine, R. Scholten, I. McNulty, K. A. Nugent, and A. G. Peele, “Dynamic sample imaging in coherent diffractive imaging.” Opt. Lett. **36**, 1954–1956 (2011).
33. T. Popmintchev, M.-C. Chen, D. Popmintchev, P. Arpin, S. Brown, S. Ališauskas, G. Andriukaitis, T. Balčiunas, O. D. Mücke, A. Pugzlys, A. Baltuška, B. Shim, S. E. Schrauth, A. Gaeta, C. Hernández-García, L. Plaja, A. Becker, A. Jaron-Becker, M. M. Murnane, and H. C. Kapteyn, “Bright coherent ultrahigh harmonics in the keV x-ray regime from mid-infrared femtosecond lasers.” Science **336**, 1287–1291 (2012).
34. R. A. Bartels, A. Paul, M. M. Murnane, H. C. Kapteyn, S. Backus, Y. Liu, and D. T. Attwood, “Absolute determination of the wavelength and spectrum of an extreme-ultraviolet beam by a Young’s double-slit measurement,” Opt. Lett. **27**, 707–709 (2002).

35. J. C. H. Spence, U. Weierstall, and M. Howells, “Coherence and sampling requirements for diffractive imaging.” Ultramicroscopy **101**, 149–152 (2004).
36. H. M. Quiney, K. A. Nugent, and A. G. Peele, “Iterative image reconstruction algorithms using wave-front intensity and phase variation.” Opt. Lett. **30**, 1638–1640 (2005).
37. P. Thibault, M. Dierolf, A. Menzel, O. Bunk, C. David, and F. Pfeiffer, “High-resolution scanning x-ray diffraction microscopy.” Science **321**, 379–382 (2008).
38. J. W. Goodman, *Introduction to Fourier Optics* (McGraw-Hill, 1996), 2nd ed.
39. V. Elser, “Phase retrieval by iterated projections.” J. Opt. Soc. Am. A **20**, 40–55 (2003).
40. M. Born and E. Wolf, *Principles of Optics* (Cambridge University Press, 1999), 7th ed.
41. J. Kirz, “Phase zone plates for x rays and the extreme uv,” J. Opt. Soc. Am. **64**, 301 (1974).
42. G. Williams, H. Quiney, B. Dhal, C. Tran, K. Nugent, A. Peele, D. Paterson, and M. de Jonge, “Fresnel Coherent Diffractive Imaging,” Phys. Rev. Lett. **97**, 025506 (2006).
43. H. M. Quiney, A. G. Peele, Z. Cai, D. Paterson, and K. A. Nugent, “Diffractive imaging of highly focused X-ray fields,” Nat. Phys. **2**, 101–104 (2006).
44. D. Gabor, “A new microscopic principle,” Nature **161**, 777–778 (1948).
45. H. J. Kreuzer, M. J. Jericho, I. A. Meinertzhagen, and W. Xu, “Digital in-line holography with photons and electrons,” J. Phys.: Condens. Matter **13**, 10729–10741 (2001).
46. G. Koren, F. Polack, and D. Joyeux, “Iterative algorithms for twin-image elimination in in-line holography using finite-support constraints,” J. Opt. Soc. Am. A **10**, 423–433 (1993).
47. “CXRO X-Ray Interactions With Matter,” http://henke.lbl.gov/optical_constants/.
48. M. E. Siemens, Q. Li, R. Yang, K. A. Nelson, E. H. Anderson, M. M. Murnane, and H. C. Kapteyn, “Quasi-ballistic thermal transport from nanoscale interfaces observed using ultrafast coherent soft X-ray beams.” Nat. Mater. **9**, 26–30 (2010).
49. D. Nardi, M. Travagliati, M. E. Siemens, Q. Li, M. M. Murnane, H. C. Kapteyn, G. Ferrini, F. Parmigiani, and F. Banfi, “Probing thermomechanics at the nanoscale: impulsively excited pseudosurface acoustic waves in hypersonic phononic crystals.” Nano Lett. **11**, 4126–4133 (2011).
50. S. Mathias, C. La-O-Vorakiat, P. Grychtol, P. Granitzka, E. Turgut, J. M. Shaw, R. Adam, H. T. Nembach, M. E. Siemens, S. Eich, C. M. Schneider, T. J. Silva, M. Aeschlimann, M. M. Murnane, and H. C. Kapteyn, “Probing the timescale of the exchange interaction in a ferromagnetic alloy.” Proc. Natl. Acad. Sci. U.S.A. **109**, 4792–4797 (2012).

DISCLAIMER

This work was supported by the Director, Office of Science, of the U.S. Department of Energy under Contract No. DE-AC02-05CH11231.